Advances in Science and Technology Research Journal

Advances in Science and Technology Research Journal, 2027, 21(1), 103–127
https://doi.org/10.12913/22998624/231212
ISSN 2299-8624, License CC-BY 4.0

Received: 2026.07.27
Accepted: 2026.11.15
Published: 2026.12.01

Stiffness assessment of nested lattice architectures: Gains, limits, and design rules for node-coincident polymer lattices

Mikołaj Kazimierczak[1*], Mirosław Bocian[1,2]

[1] Department of Mechanics, Materials and Biomedical Engineering, Wrocław University of Science and Technology, Smoluchowskiego 25, 50-370 Wrocław, Poland
[2] Center for Materials Engineering and Metal Forming, Wrocław University of Science and Technology, Wybrzeże Wyspiańskiego 27, 50-370 Wrocław, Poland
* Corresponding author's e-mail: mikolaj.kazimierczak@pwr.edu.pl

ABSTRACT

Node-coincident nesting superimposes two lattice families onto a single periodic grid so that their struts merge at shared nodes into a single monolithic frame, printable under the same rules as its parents. This work quantifies the effect of such nesting on the initial compressive stiffness – the property that governs deflection-limited use of lattice cores – at equal nominal total relative density. An experimentally anchored modelling chain is built on compression tests of four stereolithography-printed families (simple cubic, face-centred cubic, diamond, and fluorite) at relative densities of 10% and 20%. Three model fidelities – a beam model, a node-compensated beam model, and a full solid model – use a global effective modulus, a global effective diameter correction, and topology-specific node-compensation parameters. The calibrated compensated beam gives an overall mean absolute percentage error of 16% across all eight experimental configurations and approximately 23% for the held-out subset (SC-10, FC-10, and FC-20); resolved-solid comparisons are reported where available. The calibrated chain then screens seventeen candidate nested architectures and one internal-consistency case drawn from an eight-family pool that includes two cells used exclusively as guests. Embedding a stretch-dominated guest in a bending-dominated host raises the stiffness by up to +117% at equal nominal total relative density, yet no union outperforms its better parent (−25% to −77%), in agreement with Gibson–Ashby scaling: nesting redistributes mass between load-transfer mechanisms but does not create a more efficient one. Nesting is therefore a reinforcement strategy for architecture-constrained hosts, and the experimentally anchored chain enables simulation-driven screening in which testing is reserved for selected candidates.

Keywords: lattice structures, stereolithography, initial stiffness, nested lattices, finite element modelling

INTRODUCTION

Additively manufactured lattice structures have become a standard route to tailoring mechanical response at fixed material and envelope [1, 2]. For strut-based lattices the two classical design levers are the unit-cell topology and the relative density: topology decides whether deformation is stretch-dominated (struts loaded mainly axially) or bending-dominated (struts loaded mainly in bending), and this sets how stiffness and strength scale with density [3, 4]. These two levers are quickly exhausted when a topology must be chosen from a catalogue at a prescribed density, and further gains require either a new base material or a departure from the single-topology paradigm.

Combining two architectures within one volume is such a departure. Functionally graded, hybrid, and multi-morphology lattices have been characterised under quasi-static and dynamic loading [5, 6]. Interpenetrating and composite variants add a second load-bearing network to the primary frame [7, 8]. These studies consistently report that mixing load-transfer mechanisms – a stiff stretching skeleton with a more compliant

bending frame can reach property combinations unavailable to either parent alone. The variant studied here, node-coincident commensurate nesting, is the simplest and easiest to manufacture: both parent cells are generated on the same periodic grid with the same cell size, so their strut networks merge at shared nodes into a single monolithic frame, with no connector members and no transition zones. For vat photopolymerisation the nested lattice is just another strut network and is printed in the same way as its parents. Despite this simplicity, quantitative data on how nesting changes the initial compressive stiffness at equal nominal total relative density have not been reported systematically. Therefore, two questions remain open: whether a nested union can outperform its better parent at equal nominal total relative density, and whether its stiffness can be predicted reliably for printed polymer lattices.

Initial stiffness is the sizing property of deflection-limited components such as sandwich-panel cores and lattice mounts [9, 10], and of orthopaedic implants the stiffness of which is matched to bone [11]. Together with mass, it also sets the fundamental resonances, so static and vibration-mitigation performance are coupled through the same architecture [12]. Nesting redistributes the internal load paths at constant mass, which makes it a natural lever for stiffness-driven design provided its effect can be predicted reliably. In the broader context of structural and construction engineering, performance assessment encompasses not only mechanical efficiency but also environmental, economic and temporary-use considerations [28–30]. The present study, however, focuses exclusively on mechanical performance.

Reliable prediction is not trivial for stereolithography (SLA), because printed lattices differ from their nominal design. Thin struts deviate from the nominal diameter and from datasheet properties, with knock-downs reported across a wide porosity range [13] and treated probabilistically as process scatter [14]. Node-level defects [15] and defect morphology and printing-orientation effects [16] change the response further. The cure state adds to the geometry: the final modulus depends strongly on the post-curing method and conditions [17, 18]. The resins themselves and the post-curing duration of complex parts show the same sensitivity [19, 20]. A predictive SLA lattice model must therefore be anchored to experiment through an effective, as-printed material description, not nominal data.

On the modelling side, the cost of the model matters in a study that spans many configurations. Beam elements are orders of magnitude less expensive than solid models, but misrepresent the joints: stiffened vertex regions were introduced for open-cell structures [21], and the beam-versus-solid discrepancy has been documented for printed metallic lattices [22]. Compensated beam formulations systematise the correction by stiffening the strut ends [23, 24]. Homogenisation is an efficient alternative with its own limits [25, 26]. Resolved solid models and resonance-based identification give reference accuracy at high cost [27].

This study addressed both questions within a single experimentally anchored framework. The experimental basis is a quasi-static compression campaign on four SLA-printed strut families at two relative densities, from which the initial stiffness is extracted with a reproducible regression procedure. On this basis, a three-level finite element chain – a beam model, a node-compensated beam model, and a full solid model – uses a global effective modulus, a global effective diameter correction, and topology-specific node-compensation parameters; part of the experimental set is not used in any fit to experimental stiffness data and is reserved for validation. The calibrated chain then screens eighteen admissible lattice pairings (17 candidate architectures and one internal-consistency case) generated from an eight-family cell pool; each union is designed at the same nominal total relative density and judged against the better of its two parents at that density – a metric constructed to be insensitive to the material calibration. The specific contribution of this study does not lie in introducing hybrid or nested lattices as a general concept, but in the systematic evaluation of node-coincident commensurate lattice unions in which the parent networks merge directly at shared nodes, without additional connector members or transition zones. The contribution comprises four elements: (i) a density-matched, mass-fair design comparison of every union against the better parent at the same nominal total relative density, (ii) a systematic matrix of admissible host–guest combinations, (iii) an experimentally anchored beam-to-solid modelling chain, and (iv) a computationally efficient compensated-beam model for rapid screening of candidate architectures. This comparison distinguishes reinforcement of a weaker, prescribed host from a genuine improvement in stiffness efficiency over the better parent; in the

design space examined, the former is observed, whereas the latter is not. The study constitutes the screening phase of a two-phase design workflow: the model chain is calibrated once on a small set of printed base cells, simulation ranks many candidates at low computational cost, and manufacturing and testing are reserved for the top-ranked configurations.

MATERIALS AND METHODS

This section describes the experimental data set, stiffness-extraction procedure, geometry generation, finite element models, calibration protocol, and nested-design screening.

Experimental data set

This work concentrated on the initial compressive stiffness – the slope of the elastic portion of the compressive force–displacement response. The experimental foundation is a quasi-static compression campaign on SLA-printed specimens from the four base families; these measurements calibrate and validate the base-cell model chain, which is then used to evaluate the nested architectures numerically. Four strut-based topologies were tested: Simple cubic (SC), face-centred cubic (FC), diamond (DM), and fluorite (FL), each at target relative densities of 10% and 20%. The specimens were prismatic blocks of overall size 35 × 35 × 38 mm, consisting of a lattice core of 35 mm height enclosed between two solid faceplates of 1.5 mm thickness, which provided flat and parallel load-introduction surfaces. The lattice pattern was arranged with boundary half-cells, i.e., the periodic pattern is offset by half a cell with respect to the specimen faces (Figure 1). All specimens were printed from a PP-like photopolymer (SuperPP, 3DMaterials Co., Ltd.) on a Prusa SL1S Speed system, vertically and without internal supports (0.05 mm layers, 1.5 s exposure, 5 s first layer, 10 transition layers); each build job grouped all four topologies at one density to minimise process variability. After printing, the specimens were washed in isopropyl alcohol, dried for 10 min, UV post-cured for 13 min in a Prusa CW1S station, and visually inspected for print quality. Nominal material data are a Young's modulus of 1.4 GPa, a Poisson's ratio of 0.36, and a density of 1353 kg/m³. All numerical models adopt a linear elastic, isotropic material with these values, the modulus being later replaced by the calibrated effective value E_{eff} identified in the model calibration.

Figure 2 shows the unit cells of the four tested families together with the four further families that enter the numerical nesting study as guest networks; all lattices in this work are built from these eight cells.

Quasi-static compression testing

The compression response was measured on an Instron 5982 universal testing machine under crosshead-displacement control at 5 mm/min (nominal strain rate of about 2×10^{-3} s^{-1}). Specimens were placed centrally between flat platens with the faceplates normal to the loading axis, seated with a small preload, and loaded at room temperature to well beyond the first force peak. Two to four nominally identical specimens were tested per configuration; each response was characterised in force–displacement terms, and the reported stiffness of a configuration is the

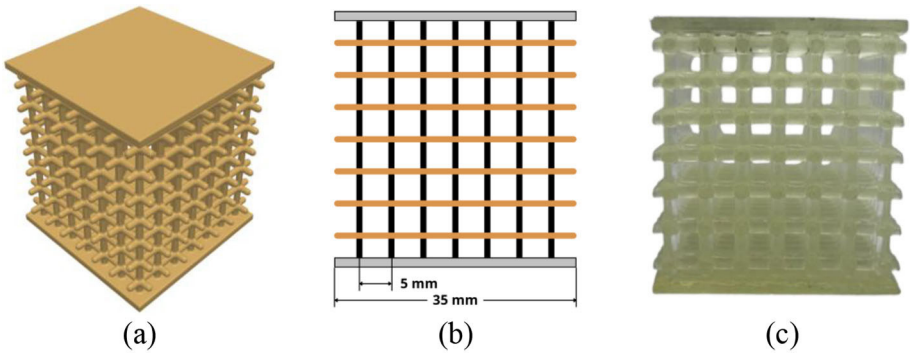


Figure 1. Specimen geometry in complementary views: (a) isometric view of the 35 × 35 × 38 mm specimen model with 1.5 mm faceplates; (b) orthographic view of the 7 × 7 × 7 cell arrangement, showing the cell size L = 5 mm and overall width (35 mm); (c) photograph of the printed SC specimen

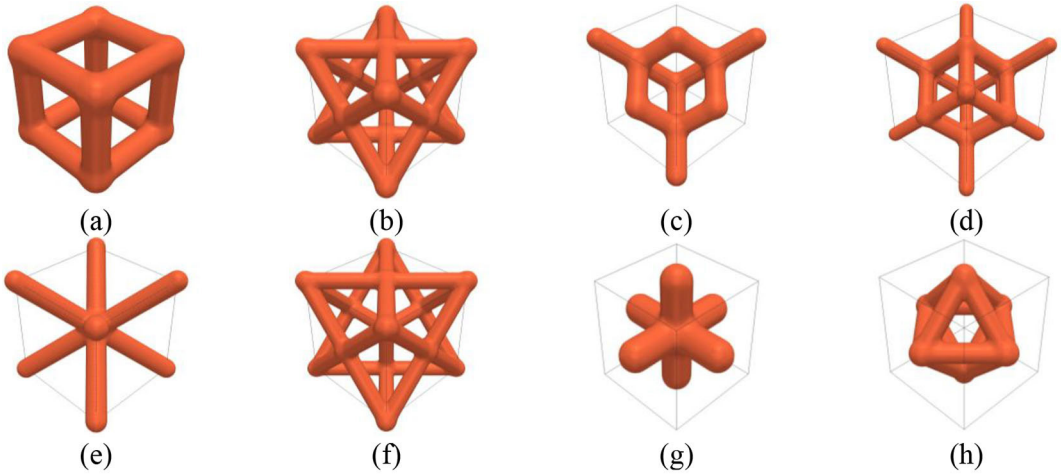


Figure 2. Unit cells of the eight strut-based families: (a) SC, (b) FC, (c) DM, (d) FL, (e) BCC, (f) OCT, (g) STAR, and (h) CUBOCT

mean over its repeats. Each raw force–displacement record was processed with the extraction procedure described below, using the high-resolution crosshead-displacement channel (10^{-5} mm resolution) to resolve the initial elastic slope.

Extraction of the initial stiffness

The initial stiffness of each specimen was defined as the steepest quasi-linear slope of its force–displacement curve before the first force peak:

$$k = \frac{\Delta F}{\Delta \delta} \tag{1}$$

where: k – initial stiffness [N/mm], ΔF – force increment over the regression window [N], $\Delta\delta$ – corresponding crosshead-displacement increment [mm].

The slope of Equation 1 was obtained using a 0.6 mm sliding-window regression on the original force–displacement record over the initial rising branch. The admissible range was identified from a lightly smoothed trace, from the seating threshold (the greater of 20 N and 2% of the pre-peak force) to the first force peak; when no distinct peak was detected, 60% of the maximum force defined the upper limit. The reported k is the steepest window with $R^2 \geq 0.995$, or the steepest admissible pre-peak window if no window met this threshold. The stiffness was evaluated per specimen and then averaged, which avoids the flattening caused by specimen-to-specimen seating offsets. The extraction is illustrated in Figure 3.

In every family, the initial stiffness increases from 10% to 20% relative density; the per-configuration stiffnesses are listed in Table 1.

Repeatability was evaluated at the configuration level using the mean, sample standard deviation, and coefficient of variation, with all repeats included. For seven of the eight configurations, the coefficients of variation ranged from 2.3% to 21.9%; FC-10 showed the largest scatter (39.7%). This measured variability is retained in the experimental error bars, and the numerical predictions are compared with configuration means, rather than fitted to individual specimens. The statistical assessment is therefore descriptive and consistent with the use of the experiments as reference targets for model calibration and validation.

Mechanism classification

The stiffnesses measured at the two densities also classify each family by its dominant deformation mechanism, through the Gibson–Ashby density exponent:

$$n = \frac{ln(k_{20}/k_{10})}{ln(\rho_{20}/\rho_{10})} \tag{2}$$

where: n – Gibson–Ashby density exponent [–]; k_{10}, k_{20} – initial stiffness at 10% and 20% relative density [N/mm]; $\rho_{20}/\rho_{10} = 2$.

Equation 2 is the two-density reduction of the Gibson-Ashby stiffness-density power law [4] – evaluated at the two densities and divided, the topology-dependent prefactor C cancels, so the exponent n follows from the two stiffnesses

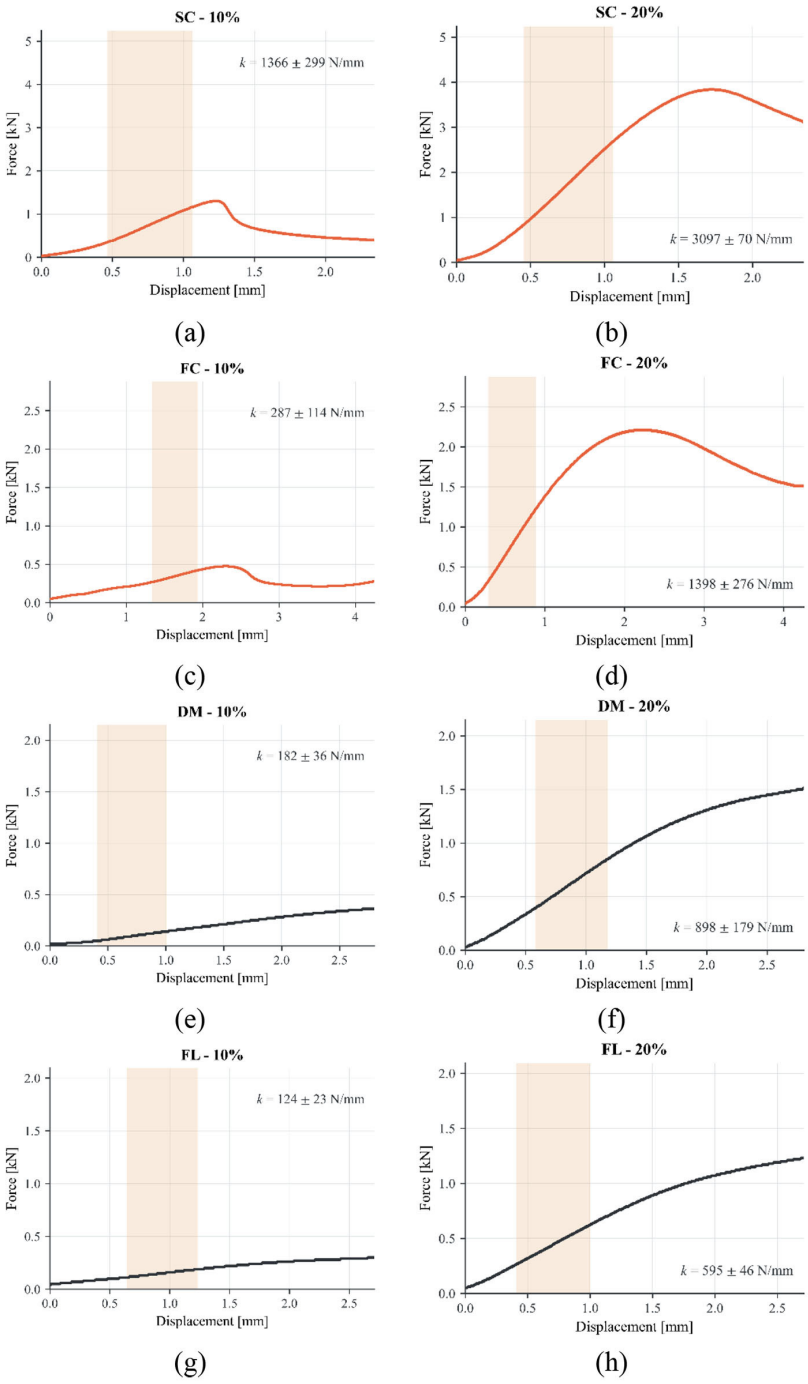


Figure 3. Representative force–displacement records for the eight tested configurations: (a) SC-10, (b) SC-20, (c) FC-10, (d) FC-20, (e) DM-10, (f) DM-20, (g) FL-10, and (h) FL-20. In each panel, the pale orange shaded area marks the regression window of the plotted specimen, while the annotation reports the corresponding configuration mean ± sample standard deviation from Table 1

alone. A cell is classified as stretch-dominated for $n < 1.5$ and bending-dominated for $n \geq 1.5$. The exponents obtained directly from the experimental mean stiffnesses are $n = 1.18$ for SC, 2.28 for FC, 2.30 for DM, and 2.26 for FL. According to the adopted threshold, SC is classified as stretch-dominated, whereas FC, DM, and FL are classified as bending-dominated. These experimental exponents should be distinguished from the model-derived exponents subsequently used to classify the complete eight-family numerical design pool. The union classifications are likewise model-derived; among them, SC⊕DM has $n = 1.498$ (shown rounded as 1.50 in Table 4), falls just below the threshold, and is classified as stretch-dominated.

Table 1. Experimental initial stiffness of the four printed lattice families at 10% and 20% relative density. Values are reported as mean ± sample standard deviation; *n* denotes the number of tested specimens

Family	Nominal ρ [%]	Number of specimens *n*	Initial stiffness k [N/mm]
SC	10	4	1366 ± 299
	20	3	3097 ± 70
FC	10	4	287 ± 114
	20	3	1398 ± 276
DM	10	2	182 ± 36
	20	2	898 ± 179
FL	10	4	124 ± 23
	20	3	595 ± 46

Lattice geometry engine and its verification

All lattice geometries in this work – experimental replicas and nested designs alike – were generated by a single in-house geometry engine. A unit cell is defined by nodes and strut connectivity on the unit cube; the specimen is obtained by tiling 7 × 7 × 7 cells of size $L = 5$ mm, clipping the struts to the specimen box, and de-duplicating shared struts and nodes. For solid models, the strut network is converted into an implicit solid: capsules along the struts are blended at the nodes into one monolithic body with smoothly filleted joints, close to the as-printed geometry. The implicit field is sampled on a uniform voxel grid, and the surface is extracted by marching cubes. For beam models, the shared nodes provide the finite element connectivity directly.

The SC and FC cells follow the standard corner-edge and corner-to-face-centre constructions; the DM and FL cells fill the interior sites of the FCC node set (Figure 2). The body-centred cubic (BCC) and octet (OCT) cells, together with the two guest-only cells STAR and CUBOCT introduced in the nesting study, complete the eight-family design pool.

The geometry engine was verified against the target relative densities. The relative density of each configuration was measured numerically on the periodic unit cell, accounting exactly for the material shared at strut intersections. All eight experimental configurations are reproduced to within 0.2 percentage points of their nominal densities (Table 2), so the generated geometries reproduce the intended nominal relative densities.

Finite element models

Three model fidelities were compared; all are linear static analyses of the same 7 × 7 × 7 specimen. In every model, the bottom face is fully constrained, and the top face is subjected to a uniform axial displacement $u_z = -0.01\ H$, with lateral motion free (Figure 4). The loaded height H is 35 mm for the beam models (the lattice core) and 38 mm for the solid model (which includes the 1.5 mm faceplates). The response is the base reaction force F, and the initial stiffness is evaluated as

$$k = \frac{F}{\delta} \tag{3}$$

Table 2. Unit-cell parameters: periodic-cell relative density measured with the as-designed strut diameters versus nominal targets

Family	Nominal ρ [%]	Design diameter d [mm]	Measured ρ [%]	Relative error [%]
SC	10	1.110	10.10	+1.0
	20	1.625	20.16	+0.8
FC	10	0.660	10.01	+0.1
	20	0.966	19.89	−0.5
DM	10	0.730	10.11	+1.1
	20	1.070	20.10	+0.5
FL	10	0.517	10.11	+1.1
	20	0.761	20.03	+0.2

where: F – base reaction force [N], $\delta = 0.01\ H$ – applied displacement [mm]. All computations were performed in Ansys MAPDL (2025 R2) driven through PyMAPDL. The three fidelities are summarised in Table 3.

Beam model

Each strut is a Timoshenko beam (BEAM188) with a solid circular section of the as-designed diameter (Table 2); struts meeting at a node share a single finite element node, i.e., the joint is rigid with full continuity of all six degrees of freedom. Model sizes range from 1 176 to 10 976 elements per specimen (Table 3), and a single solution takes on the order of one second, which makes the beam model the primary solver of the parametric study. The SC family provides an analytical check: its vertical struts form continuous columns, so the stiffness of an ideal SC lattice is the elementary column estimate

$$k_{SC} = \frac{NEA}{H} \tag{4}$$

where: k_{SC} – stiffness of the SC column lattice [N/mm], N – number of load-parallel strut columns [–], E – Young's modulus [MPa], A – strut cross-sectional area [mm²], H – loaded height [mm].

The beam solution matches Equation 4 within 1.5%, confirming the correctness of the implementation.

Node-compensated beam model

Because the beam model assigns the full nominal section along the entire strut length but ignores the extra material accumulated in the joints, it may either over- or under-estimate the stiffness depending on the topology. Locally stiffening the strut ends to represent the joints is an established remedy: Luxner et al. [21] introduced stiffened vertex regions in beam models of regular open-cell structures, and Smith et al. [22] documented the beam-versus-solid discrepancy for additively

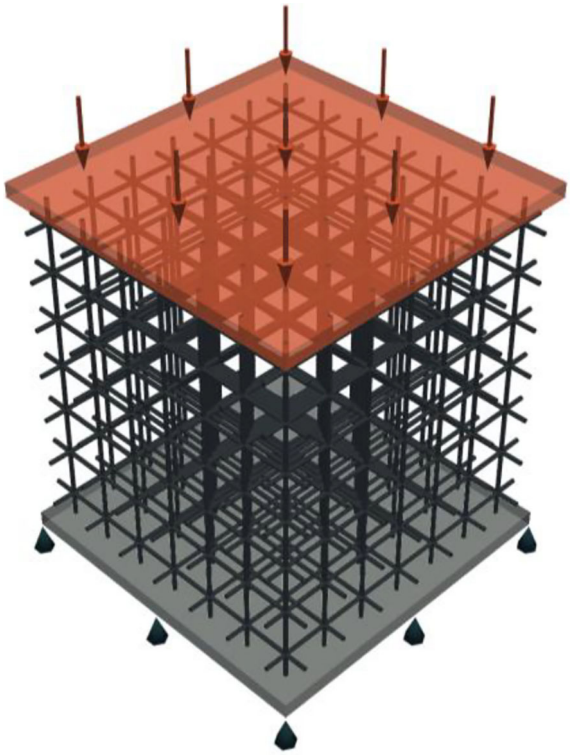


Figure 4. Boundary conditions on the 7 × 7 × 7 specimen: bottom faceplate fully fixed, top faceplate under uniform axial displacement $u_Z = -0.01\ H$, lateral motion free

manufactured metallic lattices. Recent compensated-beam formulations [23, 24] systematise the correction. In a beam model, the joint is a single point, whereas in the printed lattice, it is a solid region the size of which is comparable to the strut radius, so the real flexible length of a strut is shorter than its node-to-node distance. The compensation used here restores this: the end segments of every strut are made effectively rigid, and only the span between the joints remains flexible. The rigid length is

$$l_{rigid} = \alpha \cdot r \tag{5}$$

where: l_{rigid} – rigid end-segment length [mm], α – node-compensation parameter [–], r – strut radius [mm].

The parameter α is a dimensionless, topology-specific measure of the joint size: it states how

Table 3. Finite element models compared: element type, model size, and typical single-solution time per specimen

Model	Element type	Model size	Solution time
Beam	BEAM188 (Timoshenko)	1 176–10 976 elements	~1 s
Compensated beam	BEAM188 with rigid end offsets	1 176–10 976 elements	~1 s
Solid	SOLID187 (quadratic tetrahedra)	1.7–7.7 M nodes	6–60 min (8 cores)

far from the node the material behaves as a rigid body, in units of the strut radius. It is not a material parameter – the rigid segments are created numerically by scaling their Young's modulus to 10^3E, and the span between the joints keeps the nominal elastic section. For the families with usable solid models, the parameter α is identified by bisection against the solid model (Figure 5). Trial values are narrowed until the compensated beam matches the solid stiffness at 20% density to within 1%, and the value is then applied unchanged at 10% – a purely geometric correction, not a fit to experimental data. The identified values are $\alpha = 0.38$ (SC), 0.31 (DM), 0.20 (FL), 0.49 (FC), 0.26 (STAR), 0.38 (OCT, taken as the FC–STAR mean because no usable OCT solid model was obtained), 0.56 (CUBOCT) and 0.00 (BCC, retained as a lower bound despite a 9% residual because compensation can only stiffen); the differences reflect the different joint geometries, and all values lie below unity because the beam already carries material along the strut axis – α quantifies the equivalent extra rigid length, not the geometric extent of the joint.

Figure 6 illustrates the mechanism. The rigid length scales with the strut radius because the joint zone does – the joint is formed by overlapping cylinders of radius r – so a single α transfers across densities: thinner struts automatically attain shorter rigid ends. The correction stiffens only 7–15% of each strut length, yet, because the bending stiffness of the flexible span scales with the inverse cube of its length, it raises the strut-level bending stiffness by several tens of percent.

Solid model

The implicit geometry described above, including the 1.5 mm faceplates, is meshed with quadratic tetrahedra (SOLID187). The mesh size follows the strut diameter; the resulting models range from 1.7 to 7.7 million nodes. Mesh sensitivity was assessed for the SC-20 reference configuration,

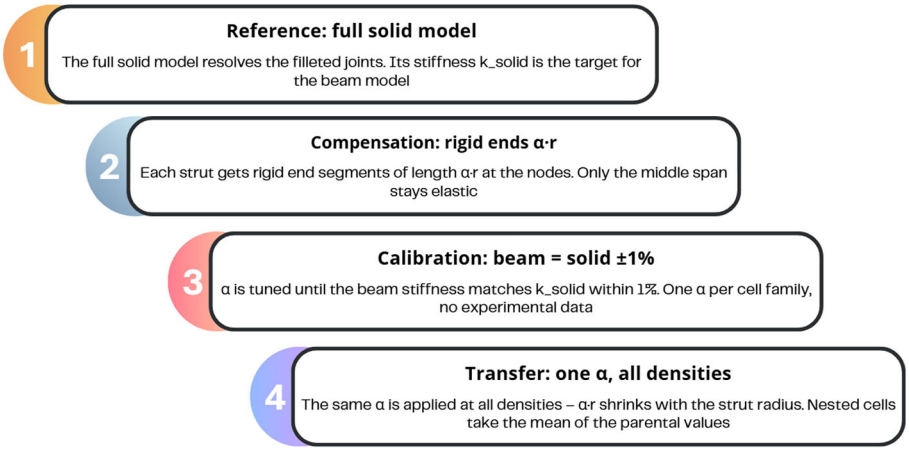


Figure 5. Construction and calibration of the compensated beam model: solid-model reference, rigid strut ends, calibration against the solid at 20% relative density, and transfer to 10% without re-fitting

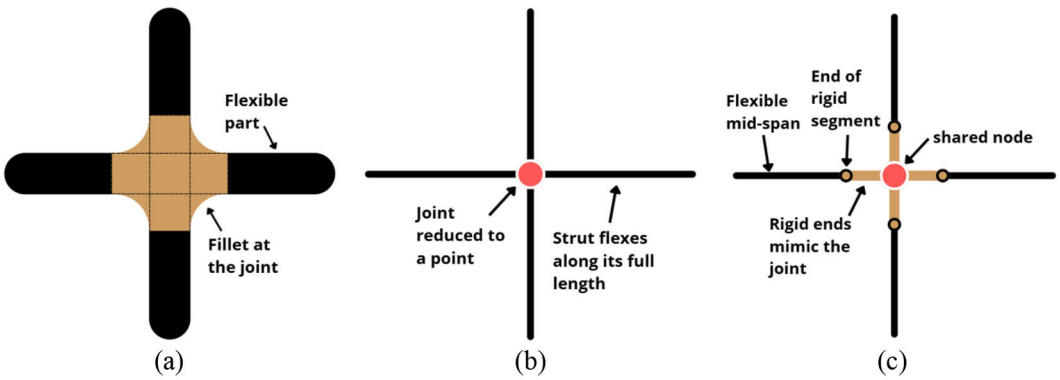


Figure 6. Node-compensation mechanism: (a) solid joint, (b) plain beam, (c) compensated beam with rigid end segments

in which mesh refinement changed the computed stiffness by 1.1%. A single solid solution takes 6–60 minutes on 8 cores, i.e. two to three orders of magnitude more than the beam model; the faceplate compliance is negligible (below 0.5% of the total). Two cells required special treatment. The FC solid could only be meshed after uniform surface remeshing (6.9 million nodes) and reproduces the FC-20 experiment to within +3.5%; at 10% density, its thinner struts could not be meshed, so FC-10 is validated by the compensated beam alone. The OCT cell could not be meshed at any tested resolution, because the octet is, by construction, the union of the FC and STAR cells, its node compensation is taken as their mean, and its resolved solid is omitted. All other families use directly meshed full solids. The finite element meshes of the three fidelities are shown in Figure 7.

Experiment-based calibration of the model chain

With nominal material data (E = 1.4 GPa) all three model fidelities overpredict the measured stiffnesses substantially, as quantified in the validation results. This is the expected behaviour of vat-photopolymerised thin-strut structures. The datasheet modulus is measured on bulk, fully post-cured coupons. The modulus of a printed feature depends on the ultraviolet dose it actually receives: Zhao et al. [17] and Cingesar et al. [18] showed strong dependence of stereolithography-part properties on the post-curing method and conditions. Riccio et al. [19] showed the same sensitivity for the resins themselves, and Guttridge et al. [20] for the post-curing duration of complex printed geometries. Inside a lattice, the dose is further limited by UV shadowing, and the partially cured surface skin takes up a large fraction of a sub-millimetre strut cross-section. Thin struts are therefore systematically more compliant than bulk coupons: Peloquin et al. [13] report such knock-downs across a wide porosity range, and Drucker et al. [14] treat the resulting variability probabilistically. Lozanovski et al. [15] and Amirian et al. [16] trace the accompanying defects. Identifying effective properties from tests on the structure itself is the

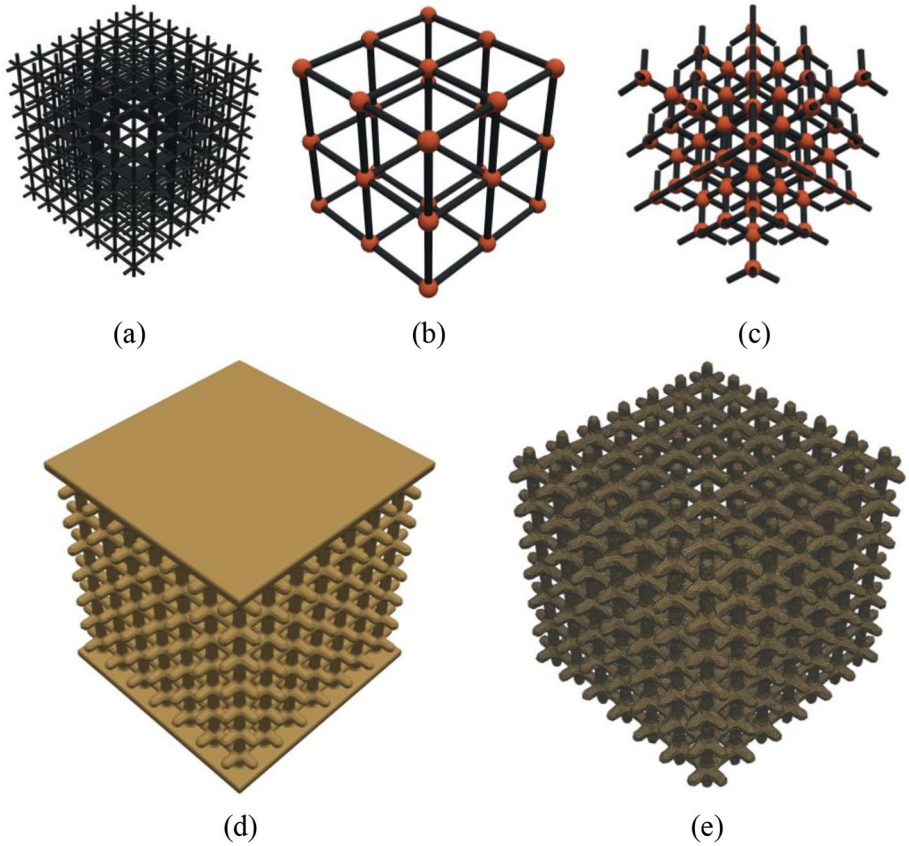


Figure 7. Finite element meshes: (a) plain beam model, one element per strut; (b) shared-node detail; (c) compensated beam with rigid end segments in amber; (d) SC-20 solid model; (e) tetrahedral mesh of the 35 mm core, shown at a coarsened 1 mm element size for visibility

established remedy: De Biasi et al. [23] calibrate an effective beam representation against reference solutions, and Fisher et al. [27] identify octet-lattice elasticity from resonance. Schneider and Kumar [31] show that the same microarchitecture printed by three processes yields three different stiffnesses, ruling out any process-independent datasheet value.

The study therefore follows a calibrate-then-predict protocol. The model chain is first calibrated against the experimental stiffnesses of the base cells; only the calibrated chain is then used for the nesting study. The calibration uses three classes of calibration and correction parameters, assigned sequentially as follows:

1. The global effective modulus E_{eff} of the as-printed material, identified from SC-20. E_{eff} is anchored on a configuration the mechanics of which the models capture closely, so that it sets the global stiffness scale with limited sensitivity to topology-dependent corrections. SC satisfies this in three ways. Its response is purely axial and follows Equation 4, so the model error is negligible – the beam, solid and analytical estimates agree within 2%. Its axial stiffness scales with d^2 , which makes SC the family least sensitive to the printed-diameter deficit. Finally, SC-20 has the thickest struts and the lowest scatter (coefficient of variation about 2%). The result, E_{eff} = 903 MPa (64.5% of nominal), is a single value applied to every geometry – one resin, one process. The geometry-dependent part of the deficit is carried by the separate, equally global Δd.
2. The node-compensation parameter α of the beam model, identified by beam–solid matching at 20% density, where a usable solid model is available. This is a purely geometric correction of the joint representation, independent of E and transferable across densities; it is not a fit to the experiment. With the identified values (α = 0.00–0.56), the compensated beam matches the solid stiffness at 20% density to within 1% for every directly meshed family except BCC. The plain BCC beam already exceeds its solid by 9%, and since the compensation can only stiffen, α = 0 is its lower bound; this 9% residual is carried into the nesting predictions for BCC-containing unions.
3. The global empirical diameter correction Δd: in the compensated-beam chain, every strut is modelled with the diameter $d - \Delta d$ instead of the as-designed d. This represents an effective reduction in load-bearing diameter associated with thin-feature dimensional deviations and surface effects; it may also absorb residual model-form error. A thinner strut loses bending stiffness ($\propto d^4$) about twice as fast as axial stiffness ($\propto d^2$), so an overprediction confined to the bending-dominated families is the signature of a diameter deficit – exactly the residual left after E_{eff}. A single global Δd, fitted on DM and FL at 10% and 20%, is 120 µm; it reduces the mean error over these four fit targets from 78% to 11.5%. Δd acts within the compensated-beam chain only; the solid model is kept at the as-designed geometry as an independent diagnostic. E_{eff} and Δd are coupled effective calibration parameters that absorb material, geometric, and model-form effects rather than uniquely identified physical quantities.

The split between calibration and validation is explicit. Calibration uses SC-20 (for E_{eff}) and DM and FL at both densities (for Δd); α involves no experimental data. SC-10 and FC at both densities take no part in any fit to experimental stiffness data and serve as held-out experimental validation targets. Since all models are linear in E, E_{eff} acts as a pure scale factor, and the gain metric of the nesting study is independent of it altogether.

Possible bias associated with identifying E_{eff} from SC-20 alone was examined through an alternative joint relative-least-squares fit to SC-20, DM-10/20, and FL-10/20. The objective minimised the sum of squared relative stiffness errors over these five configurations. The joint fit gave E_{eff} = 1070 MPa and Δd = 155 µm, compared with 903 MPa and 120 µm in the sequential calibration. The calibration-set, held-out, and all-eight mean absolute percentage errors changed from 12.2%, 22.8%, and 16.2% to 10.0%, 19.0% and 13.4%, respectively. The directed host-gain ranking was essentially unchanged (Spearman rank correlation 0.998; maximum gain change 8.2 percentage points). Thus, the SC-20 anchor does not control the screening conclusions. Because the joint fit trades off E_{eff} and Δd, the sequential calibration is retained as the baseline, whereas the joint fit is used only as a robustness check.

The transferability of Δd was tested separately while retaining the baseline E_{eff} = 903 MPa. Applied to DM and FL at both densities, the baseline Δd = 120 µm gave a mean absolute percentage error of 11.5%. Fits to individual families or density levels gave 100–160 µm.

Here, transfer error denotes the mean absolute percentage error obtained when a subset-fitted Δd was applied without refitting to the complementary family or density subset; these errors ranged from 12.0% to 27.8%. The single global Δd is therefore retained as a screening-level correction over the investigated range, not as a demonstrably density-independent or uniquely physical diameter deficit. The complete protocol is summarised in Figure 8.

Nesting study design

The nesting study uses a fixed host–guest convention. The host (the base) is always one of the four tested families – SC, FC, DM, or FL – the outer, experimentally characterised load-bearing frame. The guest is a second strut network embedded inside the host on the same 5 mm periodic grid, so the two networks share nodes wherever their node sets overlap. The nested lattice is their union with duplicated struts removed (Figure 9).

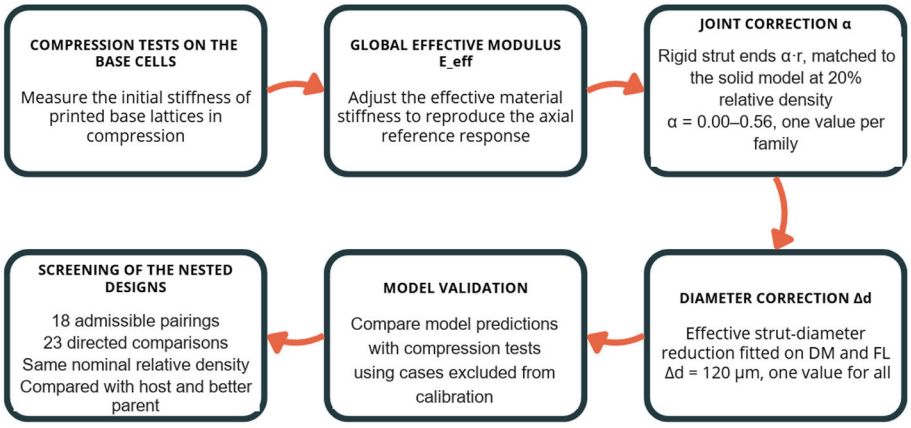


Figure 8. Calibration protocol: a global effective modulus, a global effective diameter correction, and topology-specific node compensation anchor the base-family workflow; held-out base configurations are then tested before numerical screening of nested unions

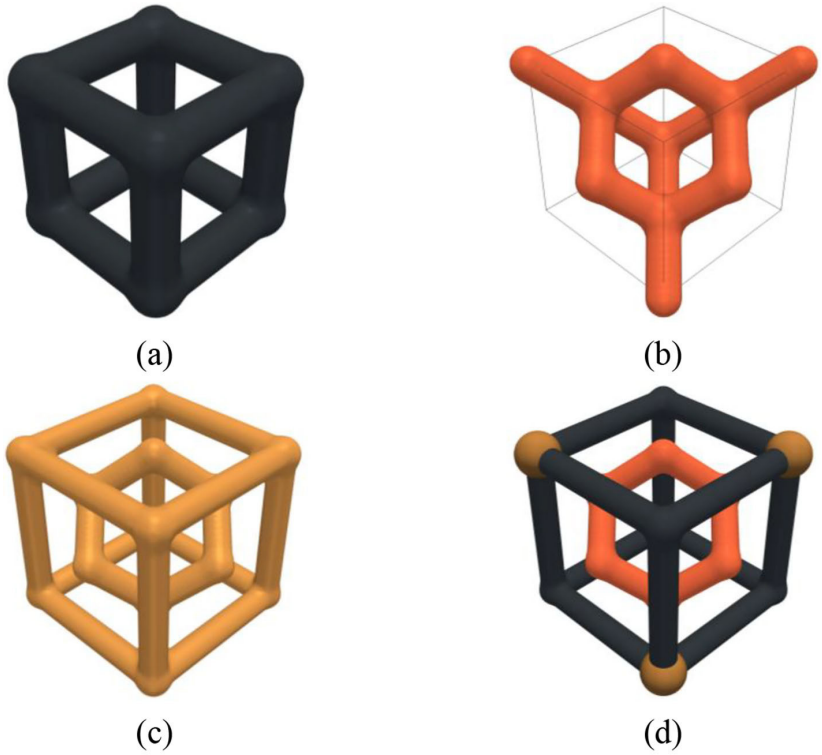


Figure 9. Node-coincident nesting (SC⊕DM): (a) host, (b) guest, (c) union merged at shared nodes, (d) coupling detail

No connector struts are introduced anywhere in the design space: the parent networks are coupled exclusively through their coincident nodes. In all nesting figures, the host struts are drawn in charcoal, the guest struts in coral, and the coincident nodes as amber spheres.

The guest pool comprises eight families: the four experimental ones, the classical BCC and OCT cells, and two cells used exclusively as guests, STAR and CUBOCT (Figure 2g,h).

The selected pool is mechanism-balanced rather than exhaustive: it combines four experimentally anchored hosts with canonical stretch- and bending-dominated cells and guest networks that generate corner, face-centre and cell-centre coupling. It does not statistically represent the wider space of sheet-based, triply periodic minimal-surface, stochastic, graded, or non-commensurate lattices. The conclusions, therefore, apply to the investigated class of commensurate node-coincident strut networks. Table 4 catalogues the 22 unique host–guest pairs and applies two admissibility tests: the union must form a single connected body, and neither parent may contain the other.

Four pairs fail these tests. Two are degenerate (DM $\subset$ FL and FC $\subset$ OCT), and two are disconnected (SC$\oplus$STAR and SC$\oplus$CUBOCT: SC occupies only cell corners, while STAR and CUBOCT occupy only face and cell centres). The remaining eighteen admissible pairings, listed once as unordered pairs, are: SC $\oplus$ {FC, DM, FL, BCC, OCT}; FC $\oplus$ {DM, FL, BCC, STAR, CUBOCT}; DM $\oplus$ {BCC, OCT, STAR, CUBOCT}; FL $\oplus$ {BCC, OCT, STAR, CUBOCT}.

Table 4. Host–guest pairs: coincident-node coupling, the two admissibility tests, and the eighteen admissible pairings listed once each. The union class follows Equation 2; SC$\oplus$DM (n = 1.498, shown rounded as 1.50) falls just below the classification threshold and is classified as a stretch-dominated

Pair (host $\oplus$ guest)	Shared nodes per cell	Node type	Single connected body	One parent contains the other	Studied	Union class (n)
FC $\oplus$ FL	7.9	Corners + face centres	Yes	No	Yes	Bending (1.98)
FL $\oplus$ OCT	7.9	Corners + face centres	Yes	No	Yes	Bending (1.68)
FC $\oplus$ DM	7.4	Corners + face centres	Yes	No	Yes	Bending (1.87)
DM $\oplus$ OCT	7.4	Corners + face centres	Yes	No	Yes	Bending (1.66)
FC $\oplus$ STAR	4.5	Face centres	Yes	No	Yes	Stretch (1.48)
FC $\oplus$ CUBOCT	4.5	Face centres	Yes	No	Yes	Bending (1.60)
DM $\oplus$ STAR	4.5	Face centres	Yes	No	Yes	Bending (1.52)
DM $\oplus$ CUBOCT	4.5	Face centres	Yes	No	Yes	Bending (1.87)
FL $\oplus$ STAR	4.5	Face centres	Yes	No	Yes	Bending (1.69)
FL $\oplus$ CUBOCT	4.5	Face centres	Yes	No	Yes	Bending (2.02)
SC $\oplus$ FC	3.4	Corners	Yes	No	Yes	Stretch (1.47)
SC $\oplus$ FL	3.4	Corners	Yes	No	Yes	Bending (1.69)
SC $\oplus$ BCC	3.4	Corners	Yes	No	Yes	Stretch (1.45)
SC $\oplus$ OCT	3.4	Corners	Yes	No	Yes	Stretch (1.42)
FC $\oplus$ BCC	3.4	Corners	Yes	No	Yes	Bending (1.64)
FL $\oplus$ BCC	3.4	Corners	Yes	No	Yes	Bending (2.13)
SC $\oplus$ DM	2.9	Corners	Yes	No	Yes	Stretch (1.50)
DM $\oplus$ BCC	2.9	Corners	Yes	No	Yes	Bending (2.05)
DM $\oplus$ FL	11.4	Corners + face centres	Yes	Yes	No (redundant union)	–
FC $\oplus$ OCT	7.9	Corners + face centres	Yes	Yes	No (redundant union)	–
SC $\oplus$ STAR	0.0	–	No	No	No (guest disconnected)	–
SC $\oplus$ CUBOCT	0.0	–	No	No	No (guest disconnected)	–

One configuration, FC⊕STAR, exactly reconstructs the OCT cell (the FC corner-to-face-centre struts plus the STAR centre-to-face-centre struts). It therefore adds no new architecture and is used only as an internal consistency check of the modelling chain, not as a new design candidate. The retained configurations couple through 2.9–7.9 shared nodes per cell, at corners, face centres or both (Table 4); the role of coupling density in the stiffness gain is examined in the results. Representative configurations are shown in Figure 10.

The comparison is made at equal nominal total relative density. For every configuration, parent or nested, the common strut diameter is adjusted until the periodic-cell density equals the 10% or 20% target. The cell size, specimen dimensions, and host topology remain unchanged; only the strut diameter changes. The guest adds strut length, so holding the density fixed thins all struts of the union – the host donates material to the guest. For the common material and specimen envelope, this is a mass-fair design comparison based on nominal periodic-cell density, not on measured as-printed mass: keeping the strut diameter would add material with every guest, and rescaling the host dimensions would change the specimen itself. The primary metric is the stiffness gain relative to the better parent at the same density:

$$G = \frac{k_{\text{nested}} - max(k_A, k_B)}{max(k_A, k_B)} \times 100\% \quad (6)$$

where: G – stiffness gain over the better parent [%], k_{nested} – stiffness of the union [N/mm], k_A, k_B – stiffnesses of the two parents at the same relative density [N/mm].

The gain G over the better parent is orientation-independent and insensitive to the effective-modulus calibration. By contrast, gain over the host is directed: the 18 admissible pairings yield 23 comparisons because five unions of two tested families are evaluated with either parent as host. Figure 17 uses all 23 directed cases (group sizes 8, 1, 10, and 4); FC⊕STAR remains among the 18 as an internal consistency check. The full matrix – 18 admissible pairings plus 8 parents, at two densities – is computed with the calibrated compensated beams. The compensation of a nested configuration is taken as the mean of its

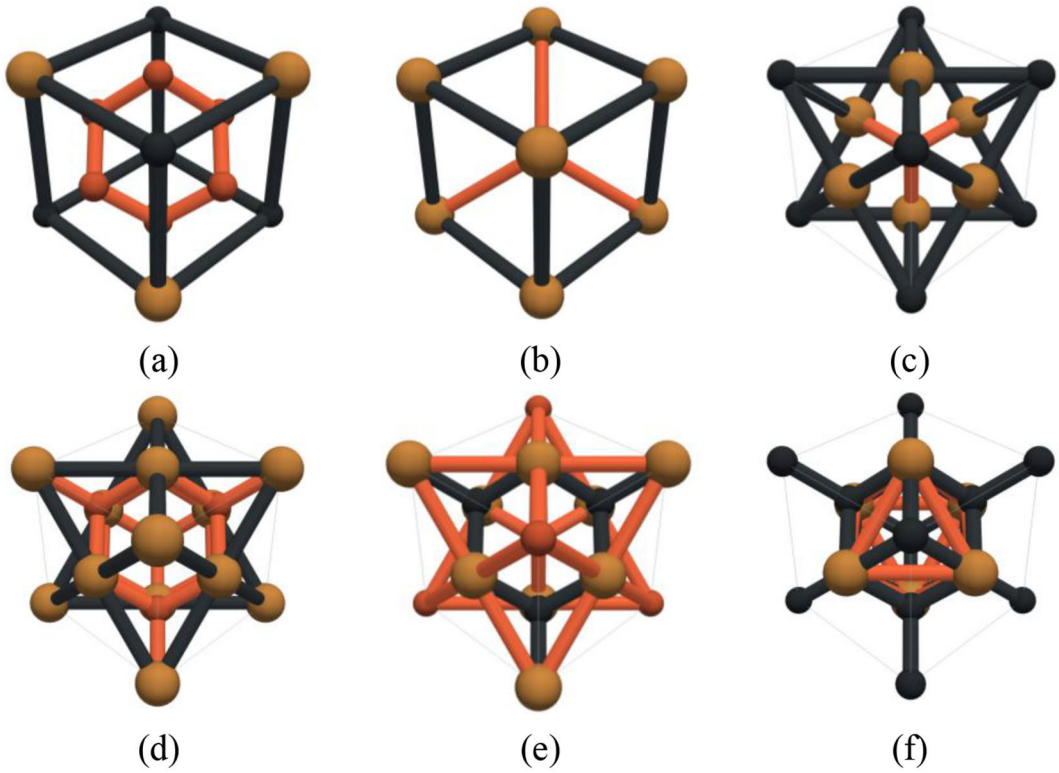


Figure 10. Representative nested configurations (host in charcoal, guest in coral, coincident nodes in amber): (a) SC⊕DM and (b) SC⊕BCC, corner coupling; (c) FC⊕STAR, face-centre coupling and exact reconstruction of OCT; (d) FC⊕FL and (e) DM⊕OCT, corner-plus-face-centre coupling; (f) FL⊕CUBOCT, face-centre coupling

two parental α values, and the strongest configurations are additionally verified with full solid models. As a robustness check, the whole matrix is also evaluated without Δd; the outcome is reported in the results.

RESULTS

The results are presented in three stages: experimental stiffness, validation of the model chain, and stiffness trends across the nested-design matrix.

The measured initial stiffness spans a factor of 25 across the eight configurations, from 124 N/mm (FL-10) to 3097 N/mm (SC-20), and rises with relative density in every family (Table 1). These are experimental means, later compared with the model predictions.

Validation of the model chain

With nominal material data, the plain (uncompensated) beam model overpredicts the experimental stiffnesses by +33% to +232%, and the solid model by +51% to +130%. As argued in the calibration, the SC family isolates this discrepancy as a material and manufacturing effect. Calibrating the single effective modulus on SC-20 gives E_{eff} = 903 MPa (64.5% of nominal), in line with the knock-downs reported for thin vat-photopolymerised features [13, 14]. Node-level defects and the post-curing route act in the same direction [15, 17]. The cure state of the resin itself shows the same sensitivity [19].

With this single scaling, the solid model becomes predictive at the target densities. The blind check on SC-10, which took no part in the calibration, deviates by only −3% from the experimental mean, well inside the specimen scatter. The bending-dominated families retain a positive residual of +15% to +48% (Table 5). The residual is largest for the thinnest struts and the most bending-sensitive family – the signature of a printed-diameter deficit acting through d^4. The full calibration closes most of this residual: with the identified family α values and Δd = 120 µm, the calibrated compensated beam gives an overall mean absolute percentage error of 16% across all eight configurations, including fit targets; the held-out SC-10, FC-10 and FC-20 errors are −21%, +22% and −25%, respectively, giving a held-out mean absolute percentage error of approximately 23% (Table 5, Figure 11).

The residual structure is informative. The single global Δd slightly over-corrects the SC columns, whose deficit was already absorbed into E_{eff}, and under-corrects the thinnest 10% struts. The residual represented by Δd increases towards the printability limit, consistent with reported defect morphology [13, 16].

Model accuracy follows both the load-transfer mechanism and nodal complexity. SC is dominated by continuous axial columns, for which the analytical, beam, and solid descriptions agree closely; after material scaling, little topology-dependent correction remains. DM and FL are bending-dominated, so their stiffness is more sensitive to strut diameter (approximately proportional to the fourth power of diameter) and to rotations at multi-strut joints. FC is a borderline case with oblique load paths and strongly connected nodal regions, making its beam idealisation especially sensitive to the effective joint length.

The close agreement of the FC-20 solid model with experiment (+3.5%), contrasted with

Table 5. Calibrated model chain versus experimental stiffness at 10% and 20% relative density. The Role column marks each configuration's part in the calibrate-then-predict protocol; the SC-20 solid error is zero by construction (E_{eff} calibration target)

Configuration	k exp [N/mm]	k comp-beam cal [N/mm]	comp-beam err [%]	k solid E_{eff} [N/mm]	solid err [%]	Role
DM-10	182 ± 36	223	+23	226	+24	Δd fit
FC-10	287 ± 114	351	+22	–	–	validation
FL-10	124 ± 23	127	+3	142	+15	Δd fit
SC-10	1366 ± 299	1082	−21	1331	−3	validation
DM-20	898 ± 179	780	−13	1062	+18	Δd fit
FC-20	1398 ± 276	1043	−25	1447	+3	validation
FL-20	595 ± 46	550	−8	884	+48	Δd fit
SC-20	3097 ± 70	2631	−15	3097	+0	E_{eff} calibration

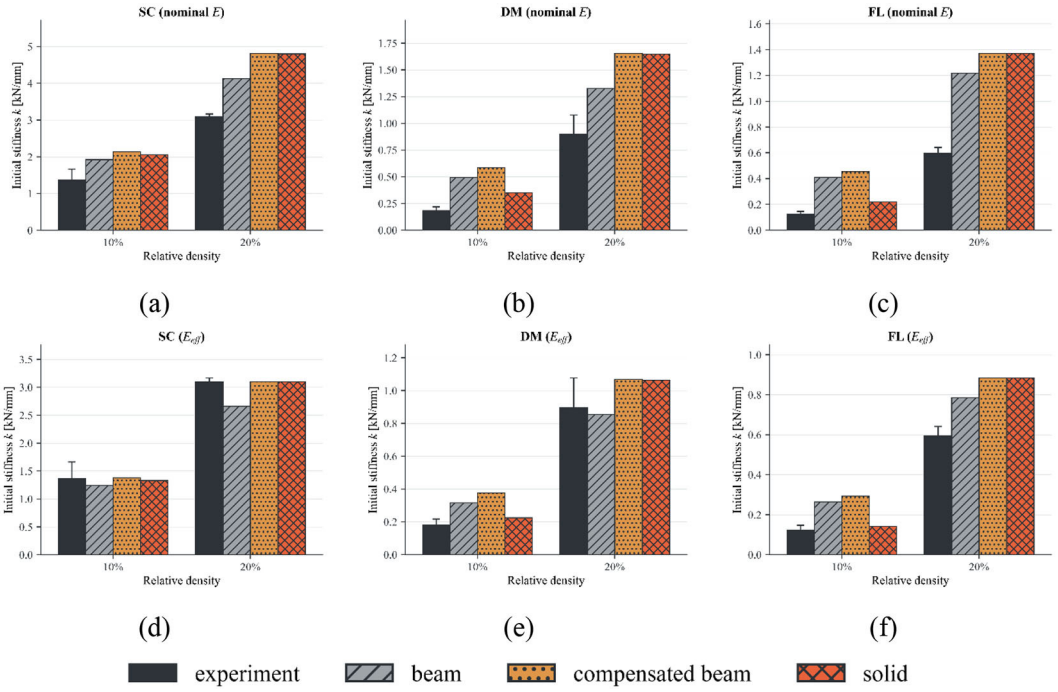


Figure 11. Base-cell stiffness at 10% and 20% relative density: SC (a, d), DM (b, e), and FL (c, f). Panels (a–c) compare the experiment with models using nominal E; panels (d–f) show the corresponding models using E_{eff}. Experimental error bars denote ±1 sample standard deviation

the −25% compensated-beam error, indicates that the dominant FC-20 discrepancy arises from the transferred Δd and/or the beam representation of the nodal region, rather than from the global modulus. For FC-10, the 39.7% experimental coefficient of variation and the absence of a resolved solid model prevent a unique attribution; thin-strut geometry, curing variability, and beam idealisation may all contribute.

Effect of nesting on the initial stiffness

Two internal consistency checks were applied to the matrix. First, the FC⊕STAR configuration reproduces the independently generated OCT lattice exactly (stiffness identical to four significant digits at both densities), so the geometric union, the diameter calibration, and the beam assembly are mutually consistent. Since α_{OCT} is by definition the FC–STAR mean, this numerical consistency check verifies the geometric union and the equal-density diameter matching rather than the compensation rule itself. Second, the gain ranking is robust to the inclusion of the manufacturing correction. Recomputing the whole matrix without Δd changes individual gains by at most 24 percentage points, but leaves the ranking essentially unchanged (Spearman $r_s = 0.99$, Figure 16b). The main ranking is therefore robust to the inclusion of the global Δd correction.

The parental-mean rule for a nested α was tested by recomputing the complete matrix with the smaller and larger parental values as bounds. Relative to the mean rule, the maximum union-stiffness change was 7.3%, the maximum change in directed mean host gain was 5.0 percentage points, and the rankings remained essentially identical (Spearman rank correlation 0.999 for both bounds). No better-parent gain changed sign. Across the same bounds, the two available nested solid checks remained within 4.5–10.4% of the beam predictions. The parental mean is therefore retained as a parsimonious screening choice, rather than treated as a direct calibration of every nested joint.

The central results are collected in the design map of Figure 12: the stiffness a guest adds to a host that is fixed by other considerations, at equal nominal total relative density. The pattern is strongly asymmetric and follows the mechanism classes of the parents, determined from the model-derived Gibson–Ashby exponents. Embedding a stretch-dominated guest (STAR, SC, or OCT) into a bending-dominated host (FC, DM, or FL) raises the stiffness by +25% to +117% at equal nominal total relative density. The STAR guest is the most effective: DM⊕STAR (+117%) and

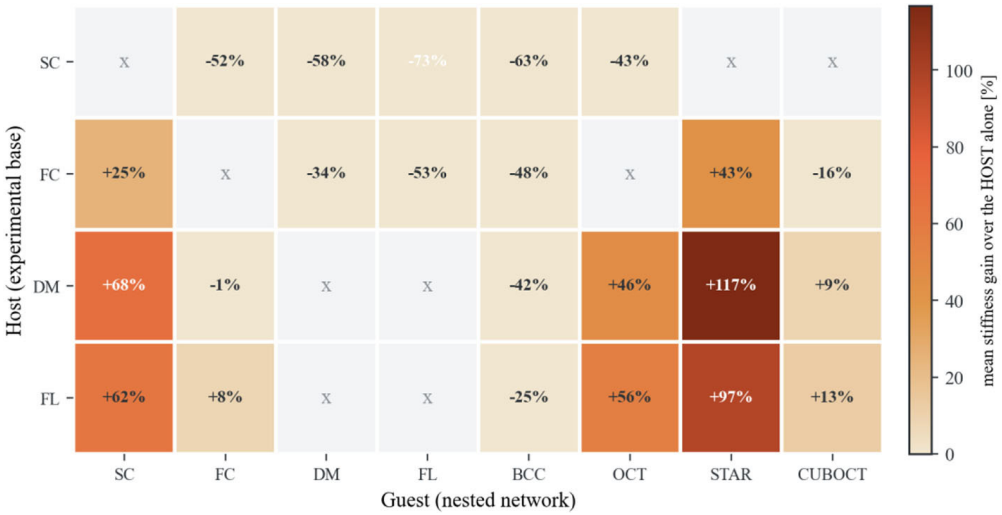


Figure 12. Nesting design map at equal nominal total relative density (mean of both densities): stiffness gain over the host. Cells marked "x" are excluded combinations

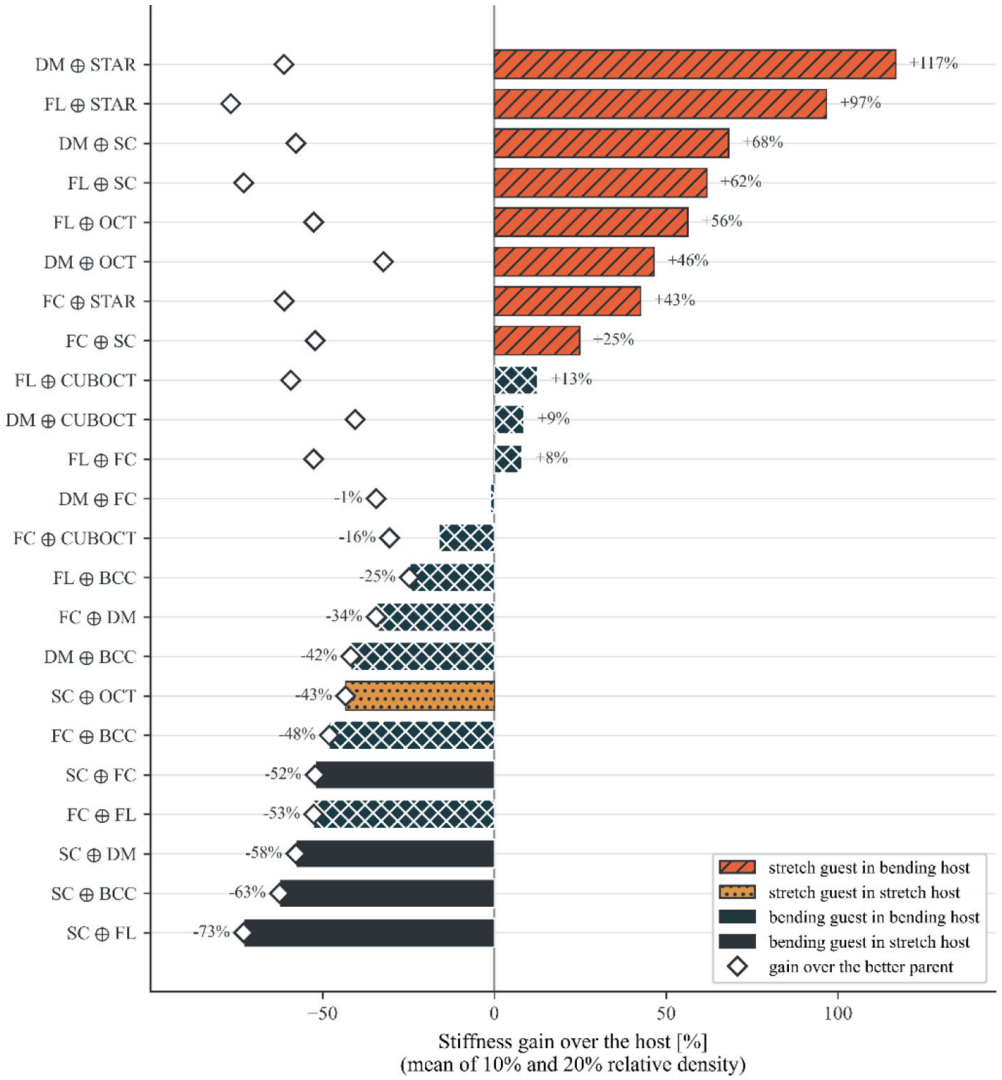


Figure 13. Ranking of 23 directed host–guest comparisons: bars – stiffness gain over the host (mean of both densities); diamonds – gain over the better parent at the same nominal total relative density, Eq. (6). Colours and hatches encode the model-derived guest-to-host mechanism classes (threshold n = 1.5). A bar that ends exactly at its diamond means the host itself is the better parent. All diamonds are negative: no union outperforms its better parent

FL⊕STAR (+97%) top the ranking (Figure 13). Among bending-dominated guests, the borderline FC (n = 1.55) and CUBOCT (n = 1.67) range from moderately negative to mildly positive in bending hosts (−16% to +13%), whereas the more strongly bending guests DM, FL, and BCC reduce the stiffness of every host (−25% to −73%). No guest improves the already stretch-dominated SC.

Figure 13 presents the same results as a ranking. Each row is one directed host–guest comparison. The bar measures the gain over the host: how much stiffer the union is than the host lattice alone. The diamond measures the gain over the better parent, Equation 6: the same union compared with the stiffer of its two parents at the same nominal total relative density. The bars show that a well-chosen guest can more than double the stiffness of a soft host. All diamonds lie below zero, showing that every better-parent gain is negative. Across the 18 admissible pairings, the better-parent gains averaged over the two densities fall between −25% and −77% (per-density extremes: −22% to −80%). Nesting can therefore strengthen a weaker lattice, but none of the investigated unions exceeds the stiffness of the stronger parent used alone.

The underlying mechanics are visualised by the deformation fields of Figure 14. At equal nominal total relative density, the common strut diameter of a union is necessarily smaller than that of either parent alone. The bending contribution of the host scales with d^4 and therefore collapses rapidly under this dilution, while the stretching contribution of the guest scales with d^2 and survives; the union thus behaves essentially as a diluted version of its stretch parent.

$$k_{bending} \propto d^4, k_{axial} \propto d^2 \quad (7)$$

Relative to a bending host, this is a large improvement: the guest supplies the axial load path the host lacks. In the pure host, the axial displacement decays unevenly through the height, because the softest layers absorb most of the compression; with the guest's straight load paths, the field becomes an almost linear gradient (Figure 14). At 20% density, the DM⊕STAR union carries a 1.9 times higher reaction force than the DM host at the same nominal total relative density.

The axial-stress maps of Figure 15 show the same mechanism, strut by strut – in FL⊕STAR, the vertical members of the guest carry the load as continuous compression columns while the host is lightly stressed, whereas in SC⊕DM, the guest carries almost no axial stress (inactive mass).

Figure 16a quantifies this. In every positive-gain union, the guest carries an axial-force share 1.3 to 3.4 times its mass share; the STAR and SC guests transmit 49–74% of the axial flow with only 18–36% of the mass. In the SC-host combinations, the relation inverts: the guest absorbs 70–82% of the mass, yet its load share never reaches its mass share. Relative to the stretch parent itself, the same dilution is a net loss, because part of the mass goes into a network that adds little stiffness. Both observations are consistent with the same Gibson–Ashby scaling.

The 23 directed host–guest comparisons derived from 18 admissible pairings were grouped by model-derived guest-to-host mechanism class using Table 6 (Figure 17). FC, with n = 1.55, was retained in the bending-dominated class according

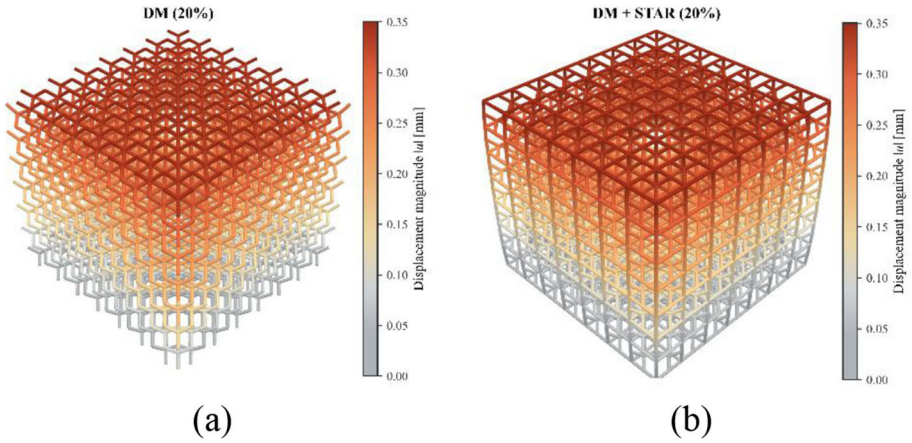


Figure 14. Deformed shapes at 1% compression: (a) DM host with an uneven axial gradient; (b) DM⊕STAR at the same nominal total relative density with a near-linear gradient

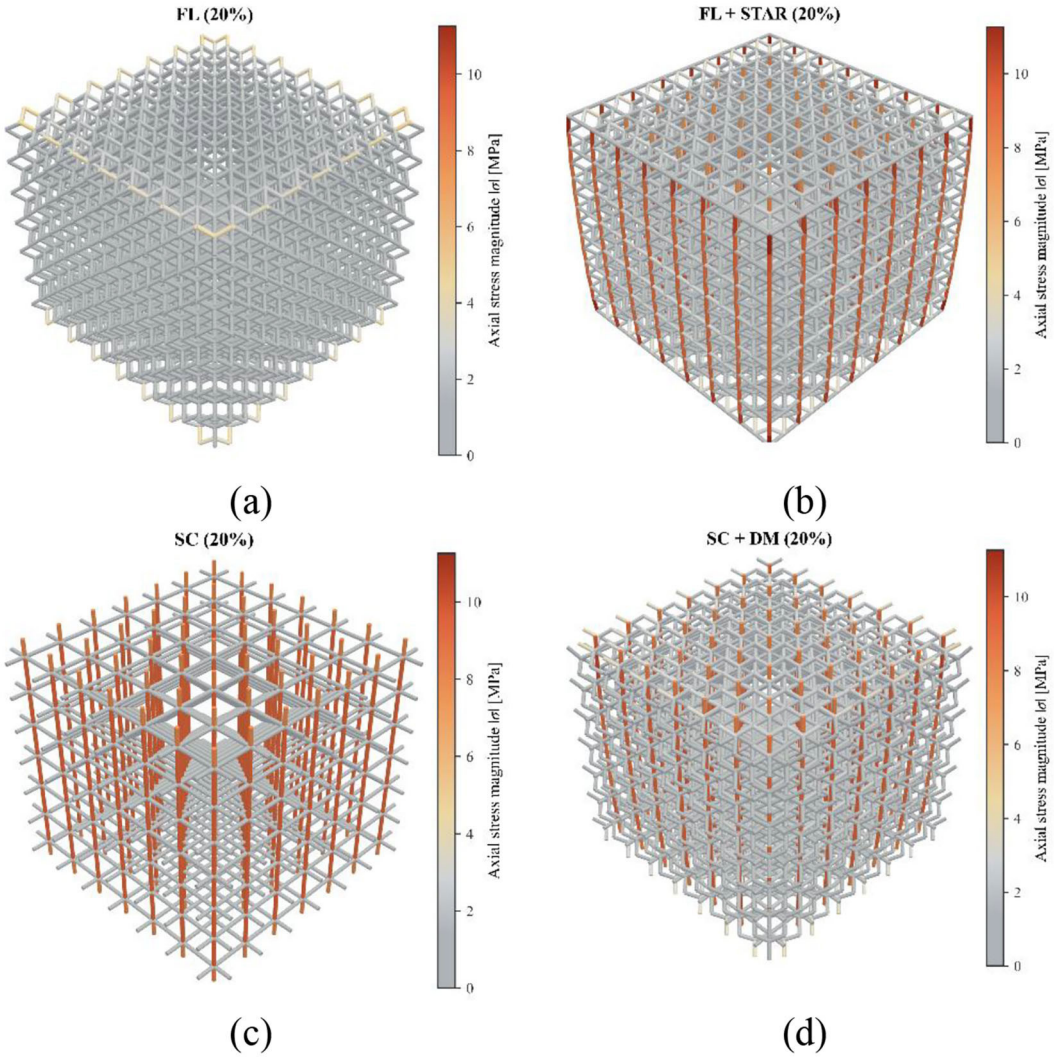


Figure 15. Axial stress at 20% density: (a, b) FL host and FL⊕STAR; (c, d) SC host and SC⊕DM

to the adopted threshold. Stretch-dominated guests in bending-dominated hosts give the only positive group mean: +64% (range +25% to +117%, n = 8). The stretch-to-stretch class is represented by a single configuration (−43%) and is not interpreted as a multi-case group estimate. The other means are −19% for bending guests in bending hosts (range −53% to +13%, n = 10) and −61% for bending guests in stretch hosts (range −73% to −52%, n = 4). This threshold-consistent assignment of FC does not alter the qualitative conclusion that stretch-dominated guests are most effective when introduced into bending-dominated hosts. Within this positive-gain group, the STAR guest, coupled only through face centres, outperforms OCT guests with about twice as many coincident nodes. Within the investigated set, the gain is associated more strongly with the straight axial load paths introduced by the guest than with the number of coincident junctions. Beam–solid cross-model verification of two nested unions at 20% relative density gave deviations of +6% for DM⊕STAR and +9% for SC⊕DM. The full screening set comprised 52 compensated-beam solutions and required only a few minutes on the workstation. Based on the measured 6–60 min per solid solution, an equivalent solid-model matrix would require approximately 5–52 h, excluding remeshing attempts and non-meshable cases.

DISCUSSION

The validation highlights two points relevant to the interpretation of printed polymer lattices. The first concerns the validation of such structures. With nominal properties, even a geometrically exact solid model of a defect-free column lattice

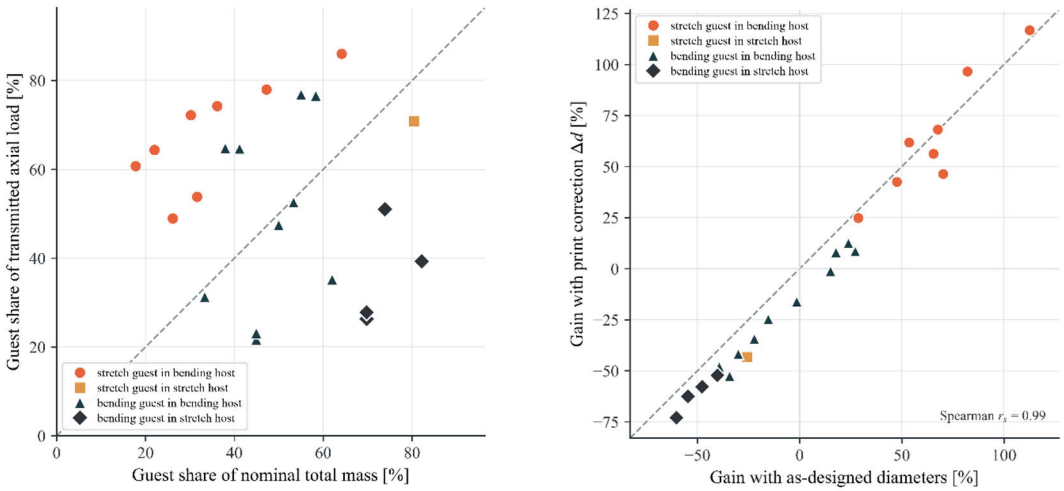


Figure 16. (a) Guest share of the axial-force flow versus guest share of the nominal total mass; (b) gains with and without Δd. Colours and markers encode the model-derived guest-to-host mechanism classes (threshold n = 1.5)

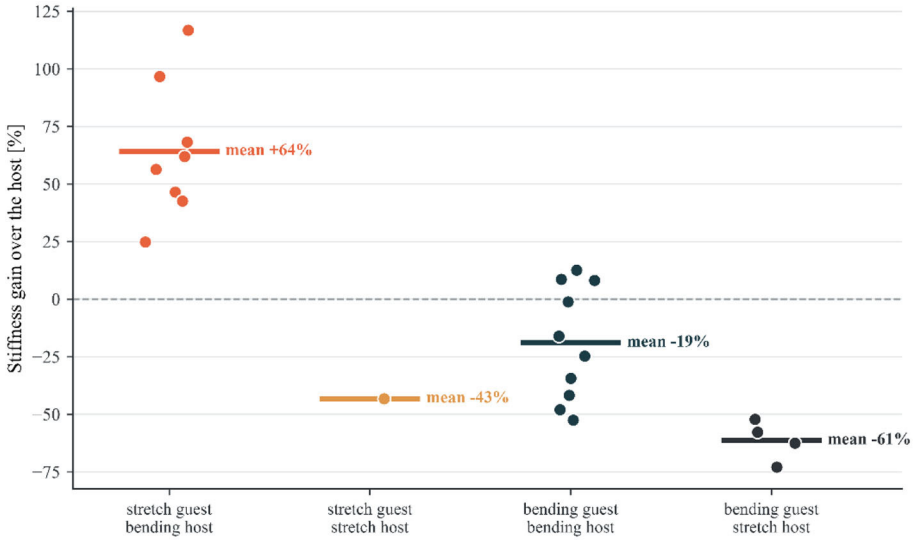


Figure 17. Stiffness gain over the host for 23 directed comparisons grouped by the model-derived guest-to-host mechanism class (threshold n = 1.5; group means marked; the stretch-to-stretch class contains one case)

overpredicts the measured stiffness by ≈55%; agreement obtained without material calibration could therefore be misleading. A single-parameter effective modulus, calibrated on the most repeatable configuration and applied without further adjustment elsewhere, is a parsimonious correction consistent with the data. Its magnitude (64.5% of nominal) quantifies the combined effect of as-printed geometry deviations, surface skin, incomplete conversion, and test-frame effects without attempting to separate them. The second finding concerns the trade-off between model fidelity and computational cost. The compensated beam model, calibrated once per family against a single solid solution, reproduces the solid predictions within 1% at the calibration density. Applied unchanged across densities, it remains computationally efficient; selected nested unions are supported by beam–solid cross-model verification within the base-cell error envelope. This is consistent with dedicated beam-compensation studies [23, 24] and complements homogenisation-based approaches [25, 26] for the nested topologies considered here.

The nesting results can be interpreted within the classical framework of cellular solids [3, 4]. The calibrated parents reproduce the two canonical scaling regimes (stretch $n \approx 1.2$, bending $n \approx 1.9$ –2.0; the experimental exponents run

slightly higher, as quantified below), and every nested union falls between its parents on the Gibson–Ashby map, never above the stretch envelope. Node-coincident nesting thus redistributes mass between mechanisms; within this design space it did not create a more efficient one. Consequently, the value of nesting is determined by the baseline against which it is judged. When the host is fixed by other requirements, such as energy absorption or an existing qualified design, a stretch guest is an effective reinforcement (up to +117% at equal nominal total relative density); within the investigated set, the largest gains are obtained with the strongest stretch architectures, while no simple positive relation with coupling density is observed. When the architecture itself is free to be chosen, nesting was not optimal within the investigated design space: for maximum initial stiffness at fixed nominal total relative density, the stiffest stretch-dominated family used alone is superior to every union.

This interpretation is consistent with the hybrid-lattice literature and makes the choice of baseline explicit. Reported stiffness or property gains for hybrid and multi-morphology lattices [5, 6] are, as here, gains relative to a compliant baseline rather than violations of the single-architecture bound. The same reading applies to the related topology- and mechanism-mixing studies [32, 33], and the present matrix makes that distinction explicit by mapping both baselines side by side. The FC⊕STAR union anchors the nesting concept directly in the classical literature: it reassembles exactly the octet cell of Deshpande, Fleck, and Ashby [3], so the octet truss itself can be read as a node-coincident nested lattice – a bending-prone FC frame stiffened by an internal star of axial members. Finally, the absence of a simple positive relation with coupling density within this design set complements studies of interpenetrating and connector-based designs [7, 8]: when the two networks are commensurate and merge at coincident nodes, the results are associated more strongly with load-path complementarity than with the number of junctions.

Several limitations bound the scope of these conclusions. The study addressed the initial, linear-elastic stiffness only; strength, buckling, post-yield energy absorption, and fatigue may rank the same configurations differently, and bending-dominated architectures retain well-documented advantages in energy absorption. The calibration is effective rather than mechanistic. E_{eff} and the global empirical diameter correction Δd form a coupled effective description rather than a unique material–geometry decomposition; Δd also absorbs residual model-form error, under-corrects the thinnest struts, and is tied to one printer, resin, and post-curing protocol. Topology- and density-specific corrections could improve absolute accuracy but would require additional reference calculations; the single global value was retained to keep the screening workflow efficient. The mesh-sensitivity estimate is based on SC-20; topology-specific refinement would provide a more complete uncertainty estimate for the thinnest and nested solid models. Finally, the nested architectures themselves have not been printed and tested here; the design maps are numerical predictions resting on a chain experimentally anchored and evaluated on the parent families. Printing and testing the top-ranked configurations, DM⊕STAR and FL⊕STAR in particular, is the natural next step: the confirmatory phase of the workflow, in which experiments are limited to the top-ranked candidates. Micro-CT measurements of the as-built diameters would then replace the effective Δd with a measured distribution.

Extending the model to peak strength, post-buckling, energy absorption, or failure would require geometric nonlinearity, a calibrated nonlinear constitutive law, initial imperfections, failure criteria, and new validation targets; rankings under those responses need not follow the initial-stiffness ranking [5, 6, 32, 33]. The geometry engine, equal-density comparison, and beam-to-solid workflow are transferable to other AM processes, whereas E_{eff} and Δd are process-specific, and α should be revalidated when the joint geometry or surface condition changes.

Comparison with predictive models

Three classical predictive tools are compared against the present results to establish how much of the observed behaviour could have been anticipated without finite-element analysis. First, the Gibson–Ashby scaling law:

$$\frac{E^*}{E_s} = C\left(\frac{\rho^*}{\rho_s}\right)^n \tag{8}$$

where: E^* – effective lattice modulus [MPa], E_S – solid-material modulus [MPa], $\rho^*/\rho s$ – relative density [–], C – topology-dependent prefactor [–], n – density exponent [–].

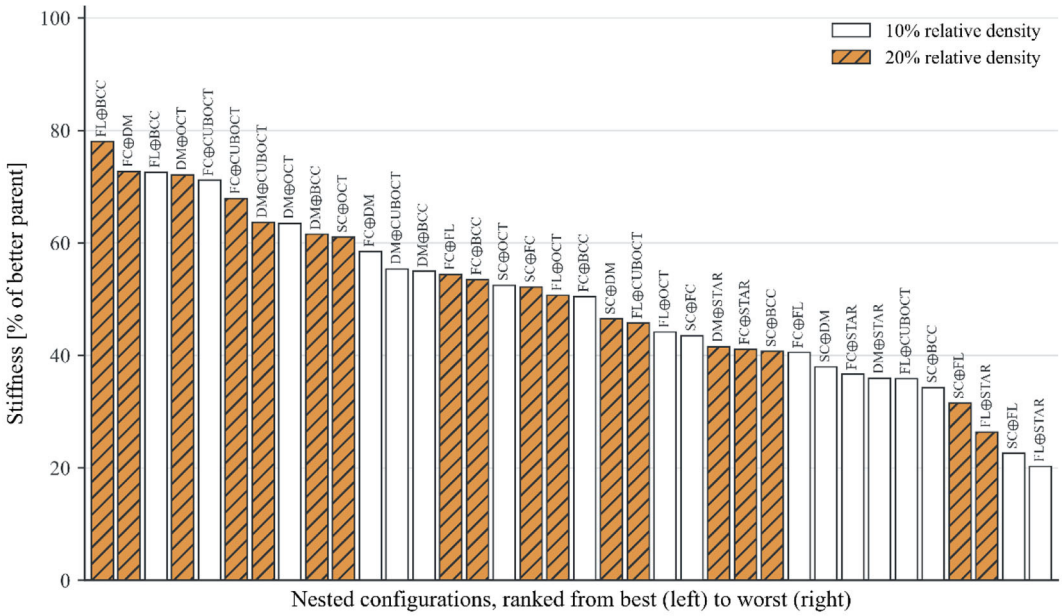


Figure 18. Stiffness of each nested pair as a percentage of its stronger parent at both densities. No bar reaches the 100% better-parent bound. Each bar is labelled with its configuration (host⊕guest); open bars – 10%, hatched bars – 20% relative density

Eq. (8) predicts n ≈ 1 for stretch-dominated cells and $n \approx 2$ for bending-dominated ones. The exponents fitted to the present data reproduce this split: $n \approx 1.2$ for SC and $n \approx 2.3$ for the bending families in the experiment, against 1.2 and 1.9–2.0 in the calibrated model. The excess of the experimental exponents reflects the diameter deficit, which penalises the thinnest struts hardest. The deformation mechanism of a cell is therefore readable from the slope of its stiffness–density curve alone. Second, the nodal-connectivity rule of Deshpande, Ashby, and Fleck [34], a Maxwell-type count of struts and joints, assigns the same classes from topology alone, before any calculation; FC is the one genuinely borderline case. Third, and most importantly, the central nesting result – no union outperforms its better parent at equal nominal total relative density – is consistent with a rule-of-mixtures argument. Dividing a fixed nominal material fraction between two strut networks behaves close to a convex combination, and the stiffest outcome of a convex combination is all the nominal material assigned in the better single network. Every computed union obeys this bound: the best pair reaches 78% of its stronger parent, the worst 20% (Figure 18). The union is not a strict convex combination of its parents, because the two networks share one rescaled diameter and

Table 6. Model-derived Gibson–Ashby density exponent n of the eight unit cells in the study, computed with the calibrated compensated-beam model on a common basis (Equation 2) and used for the unified stretch/bending classification of the full numerical design pool (threshold n = 1.5). These are not exponents obtained directly from the experiments. SC, FC, DM, and FL are the tested host families; BCC, OCT, STAR, and CUBOCT are the guest networks. FC (n = 1.55) lies just above the threshold and is retained as the borderline bending-dominated case

Unit cell	Gibson–Ashby exponent n	Classification
SC (host)	1.21	Stretch-dominated
STAR (guest)	1.31	Stretch-dominated
OCT (guest)	1.48	Stretch-dominated
FC (host)	1.55	Bending-dominated
CUBOCT (guest)	1.67	Bending-dominated
DM (host)	1.89	Bending-dominated
BCC (guest)	1.91	Bending-dominated
FL (host)	2.03	Bending-dominated

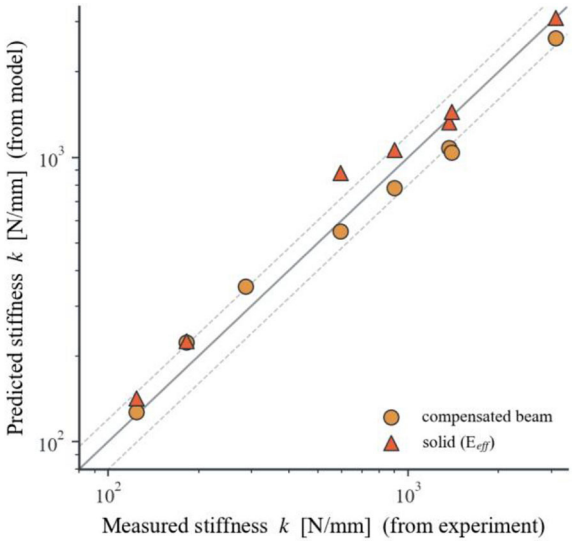
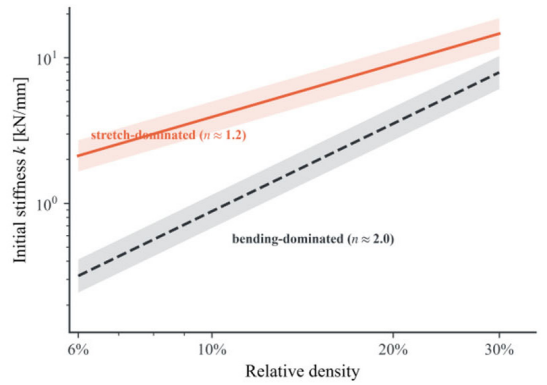


Figure 19. Predicted versus measured stiffness for the compensated beam and the full solid; dashed lines mark ±20%



(a)



(b)

Figure 20. Design-rule synthesis: (a) mean gain over the host for 23 directed comparisons by model-derived mechanism class (threshold n = 1.5; group sizes shown); (b) Gibson–Ashby reading of the nesting effect

are coupled at the nodes, so the bound is heuristic, rather than exact. The unions still gain up to +117% over the weaker host: the large positive gain over the host and the strictly negative gain over the better parent are two consequences of the same convexity argument. The exponents of all eight cells are collected in Table 6.

These predictive tools do not provide the absolute stiffness. First, the scaling law fixes only the exponent n: its prefactor C spans an order of magnitude across published lattice data for nominally identical topologies, so the law alone cannot predict a single stiffness value. Second, it is blind to the manufacturing knock-down: applied with nominal material data, it would overpredict the printed stiffness by roughly 55% (see the validation of the model chain), an error absorbed here by the calibrated E_{eff} and Δd. Third, it cannot distinguish configurations of equal density: the eighteen admissible pairings share the same relative density at each level, yet their stiffness differs by more than a factor of two, and the exponent does not rank their stiffnesses. The experiment-anchored chain addresses these three limitations: it gives an overall mean absolute percentage error of 16% across all eight configurations and approximately 23% for the held-out compensated-beam subset (Figure 19), ranks all eighteen pairings, and transfers between the two density levels without refitting. Thus, topology determines the direction of the effect – the mechanism class and the better-parent bound – while the calibrated model determines its magnitude.

Figure 20 summarises the design implications. The oriented mechanism matrix (Figure 20a) summarises the 23 directed comparisons derived from 18 admissible pairings: a stretch-dominated guest is most effective in a bending-dominated host. The quantitative grouping is reported in Figure 17 (mean +64%, up to +117%); all other pairings have negative group means. The Gibson–Ashby schematic (Figure 20b) provides the corresponding interpretation: at equal nominal total relative density a union is a diluted mixture of its parents, so nesting can lift a bending host toward the stiffer stretch envelope but never across it. Accordingly, large gains are possible relative to a fixed host, while no investigated union exceeds the better parent. Node-coincident nesting is thus a targeted reinforcement tool for constrained architectures, not a means of maximising absolute stiffness.

CONCLUSIONS

A reproducible route from raw testing-machine records to validation-grade stiffness targets was demonstrated, spanning a factor of 25 (124 to 3097 N/mm). SC-20, DM, and FL serve as calibration targets; SC-10, FC-10, and FC-20 as held-out validation targets. The lattice geometry engine was verified against the as-designed diameters of all eight experimental configurations to within 0.2 percentage points of relative density.

With nominal material data, all model fidelities overpredict the measured stiffness by 33–232%. An experiment-anchored calibration based on three classes of calibration and correction parameters gives an overall mean absolute percentage error of 16% across all eight configurations and approximately 23% for the held-out compensated-beam subset; the blind solid check on held-out SC-10 deviates by −3%. The parameter classes are: an effective printed modulus E_{eff} = 903 MPa (64.5% of nominal), identified on the column-like SC-20 configuration; a geometric node compensation α = 0.00–0.56, matching beams to solids within 1% (BCC excepted); and a global empirical diameter correction Δd = 120 µm, identified on the bending families.

Across 18 admissible node-coincident pairings (17 candidate architectures and one internal-consistency case) at equal nominal total relative density, the results are asymmetric with respect to host and guest mechanism class. Embedding a strong stretch-dominated guest (STAR, SC, or OCT) into a bending-dominated host raises stiffness by +25% to +117% (best: DM⊕STAR +117%, FL⊕STAR +97%), because the guest supplies the axial load path the host lacks; the STAR and SC guests carry 49–74% of the axial flow with 18–36% of the mass. Every other class combination reduces stiffness on average. At the same time, no union outperforms its better parent (−25% to −77%): nesting redistributes mass between mechanisms but does not beat the efficiency of the best single architecture in this design space. Nesting is therefore a reinforcement strategy for constrained hosts, not a means of maximising absolute stiffness. Within the positive-gain class, no simple positive relation with coupling density is observed: the STAR guest, attached through face centers only (4.5 coincident nodes per cell), outperforms corner-coupled alternatives. The FC⊕STAR union, which reassembles the classical octet cell exactly, serves as an internal consistency check of the geometric union and the equal-density diameter matching, and connects the nesting concept to the canonical stretch-dominated lattice of the literature.

The compensated beam reproduces solid-model stiffnesses at three orders of magnitude lower cost, enabling a two-phase workflow: calibrate once on a few tested base cells, screen many candidates by simulation, and reserve manufacturing and testing for the selected candidates. Beam–solid cross-model verification of two selected nested unions supports the transferred compensation (deviations of +6% and +9%), and the gain ranking is robust to inclusion of the global Δd correction (Spearman rs = 0.99).

Acknowledgments

The work was supported by the project Minigrants for doctoral students of the Wroclaw University of Science and Technology.

The authors would like to thank Ms. Dominika Grygier for providing access to the 3D printers and printing equipment used in this study, and Dr. Dariusz Pyka for his technical assistance during the 3D printing process.

The finite element computations were performed using an Ansys® Academic Research Mechanical license (Ansys MAPDL 2025 R2).

REFERENCES

1. Tofail SAM, Koumoulos EP, Bandyopadhyay A, Bose S, O'Donoghue L, Charitidis C. Additive manufacturing: scientific and technological challenges, market uptake and opportunities. Materials Today 2018; 21(1): 22–37. https://doi.org/10.1016/j.mattod.2017.07.001
2. Fleck NA, Deshpande VS, Ashby MF. Micro-architectured materials: past, present and future. Proceedings of the Royal Society A 2010; 466(2121): 2495–2516. https://doi.org/10.1098/rspa.2010.0215
3. Deshpande VS, Fleck NA, Ashby MF. Effective properties of the octet-truss lattice material. Journal of the Mechanics and Physics of Solids 2001; 49(8): 1747–1769. https://doi.org/10.1016/S0022-5096(01)00010-2
4. Gibson LJ, Ashby MF. Cellular Solids: Structure and Properties. 2nd ed. Cambridge: Cambridge University Press; 1997. https://doi.org/10.1017/CBO9781139878326
5. Azher K, Hussain S, Vattathurvalappil SH, Ali U, Nazir A. Buckling-stretch-buckling dominated hybrid

mechanical metamaterials fabricated from 3D-printed photopolymer: design and investigation for enhanced multifunctional mechanical characteristics. Journal of Materials Research and Technology 2025; 36: 8643-8662. https://doi.org/10.1016/j.jmrt.2025.05.077

6. Barnes BW, Babamiri BB, Demeneghi G, Soltani-Tehrani A, Shamsaei N, Hazeli K. Quasi-static and dynamic behavior of additively manufactured lattice structures with hybrid topologies. Additive Manufacturing 2021; 48: 102466. https://doi.org/10.1016/j.addma.2021.102466
7. An X, Lai C, He W, Fan H. Three-dimensional meta-truss lattice composite structures with vibration isolation performance. Extreme Mechanics Letters 2019; 33: 100577. https://doi.org/10.1016/j.eml.2019.100577
8. Li H, Hu Y, Chen J, Shou D, Li B. Lightweight meta-lattice sandwich panels for remarkable vibration mitigation: analytical prediction, numerical analysis and experimental validations. Composites Part A 2022; 163: 107218. https://doi.org/10.1016/j.compositesa.2022.107218
9. Syam WP, Wu J, Zhao B, Maskery I, Elmadih W, Leach R. Design and analysis of strut-based lattice structures for vibration isolation. Precision Engineering 2018; 52: 494–506. https://doi.org/10.1016/j.precisioneng.2017.09.010
10. Wadley HNG. Multifunctional periodic cellular metals. Philosophical Transactions of the Royal Society A 2006; 364(1838): 31–68. https://doi.org/10.1098/rsta.2005.1697
11. Zadpoor AA. Mechanical performance of additively manufactured meta-biomaterials. Acta Biomaterialia 2019; 85: 41–59. https://doi.org/10.1016/j.actbio.2018.12.038
12. Arretche I, Matlack KH. On the interrelationship between static and vibration mitigation properties of architected metastructures. Frontiers in Materials 2018; 5: 68. https://doi.org/10.3389/fmats.2018.00068
13. Peloquin J, Han Y, Gall K. Printability and mechanical behavior as a function of base material, structure, and a wide range of porosities for polymer lattice structures fabricated by vat-based 3D printing. Additive Manufacturing 2023; 78: 103892. https://doi.org/10.1016/j.addma.2023.103892
14. Drucker S, Lüdeker JK, Blecken M, Kurt A, Betz K, Kriegesmann B, Fiedler B. Probabilistic analysis of additively manufactured polymer lattice structures. Materials & Design 2022; 213: 110300. https://doi.org/10.1016/j.matdes.2021.110300
15. Lozanovski B, Downing D, Tran P, Shidid D, Qian M, Choong P, Brandt M, Leary M. Non-destructive simulation of node defects in additively manufactured lattice structures. Additive Manufacturing 2020; 36: 101593. https://doi.org/10.1016/j.addma.2020.101593
16. Amirian A, Battley M, Diegel O, Amirpour M. Additive manufacturing defects in polymeric lattice structures: a comprehensive analysis of morphology, distribution, and printing orientation influence. The International Journal of Advanced Manufacturing Technology 2025; 140(9–10): 5361–5384. https://doi.org/10.1007/s00170-025-16521-8
17. Zhao J, Yang Y, Li L. A comprehensive evaluation for different post-curing methods used in stereolithography additive manufacturing. Journal of Manufacturing Processes 2020; 56: 867–877. https://doi.org/10.1016/j.jmapro.2020.04.077
18. Cingesar IK, Markovic M-P, Vrsaljko D. Effect of post-processing conditions on polyacrylate materials used in stereolithography. Additive Manufacturing 2022; 55: 102813. https://doi.org/10.1016/j.addma.2022.102813
19. Riccio C, Civera M, Grimaldo Ruiz O, Pedulla P, Rodriguez Reinoso M, Tommasi G, Vollaro M, Burgio V, Surace C. Effects of curing on photosensitive resins in SLA additive manufacturing. Applied Mechanics 2021; 2(4): 942–955. https://doi.org/10.3390/applmech2040055
20. Guttridge C, Shannon A, O'Sullivan A, O'Sullivan KJ, O'Sullivan LW. Effects of post-curing duration on the mechanical properties of complex 3D printed geometrical parts. Journal of the Mechanical Behavior of Biomedical Materials 2024; 156: 106585. https://doi.org/10.1016/j.jmbbm.2024.106585
21. Luxner MH, Stampfl J, Pettermann HE. Finite element modeling concepts and linear analyses of 3D regular open cell structures. Journal of Materials Science 2005; 40(22): 5859–5866. https://doi.org/10.1007/s10853-005-5020-y
22. Smith M, Guan Z, Cantwell WJ. Finite element modelling of the compressive response of lattice structures manufactured using the selective laser melting technique. International Journal of Mechanical Sciences 2013; 67: 28–41. https://doi.org/10.1016/j.ijmecsci.2012.12.004
23. De Biasi R, Yasin MS, Perini M, Benedetti M, Berto F. Compensated beam model for efficient and accurate FE elastic simulation of strut-based lattice structures. Materials & Design 2025; 255: 114213. https://doi.org/10.1016/j.matdes.2025.114213
24. Gholibeygi S, Ergun H, Ayhan B. Beam finite element model modification considering shear stiffness: octet-truss unit cell with springs. Applied Sciences 2025; 15(16): 8969. https://doi.org/10.3390/app15168969
25. Kim J-E, Cho N-K, Park K. Computational homogenization of additively manufactured lightweight structures with multiscale topology optimization. Journal of Computational Design and Engineering 2022; 9(5): 1602–1615. https://doi.org/10.1093/jcde/qwac078
26. Somnic J, Jo BW. Status and challenges in homogenization methods for lattice materials. Materials 2022; 15(2): 605. https://doi.org/10.3390/ma15020605
27. Fisher K, Wang J, Tran B. Modeling and

characterizing the elastodynamic response of octet-truss lattice structures using resonance techniques. Materials & Design 2023; 226: 111688. https://doi.org/10.1016/j.matdes.2023.111688

28. Elbialy S, Youssef D, Edris WF, Ghanem G, Ibrahim W. Performance evaluation of semi-precast reinforced concrete slabs under flexural load. Civil Engineering Journal 2025; 11(12): 5032–5048. https://doi.org/10.28991/CEJ-2025-011-12-07
29. Safran M, Said I, Abuanzeh N, Baarimah AO, Abu Saleh S, Al-Zghoul TM, Mushtaha AW, Alawag AM, Alqudah S. Impact of green building strategies on environmental, economic, and social outcomes in construction. HighTech and Innovation Journal 2025; 6(4): 1449–1464. https://doi.org/10.28991/HIJ-2025-06-04-019
30. Poomchalit W, Tipboonsri P, Chongkolnee B, Pramoonmak S, Cheewawuttipong W, Memon A. Eco-friendly materials for temporary use in architecture and decorations. HighTech and Innovation Journal 2025; 6(1): 81–90. https://doi.org/10.28991/HIJ-2025-06-01-06
31. Schneider J, Kumar S. Comparative performance evaluation of microarchitected lattices processed via SLS, MJ, and DLP 3D printing methods: experimental investigation and modelling. Journal of Materials Research and Technology 2023; 26: 7182–7198. https://doi.org/10.1016/j.jmrt.2023.09.061
32. Hazeli K, Babamiri BB, Indeck J, Minor A, Askari H. Microstructure-topology relationship effects on the quasi-static and dynamic behavior of additively manufactured lattice structures. Materials & Design 2019; 176: 107826. https://doi.org/10.1016/j.matdes.2019.107826
33. Jiang W, Yin G, Xie L, Yin M. Multifunctional 3D lattice metamaterials for vibration mitigation and energy absorption. International Journal of Mechanical Sciences 2022; 233: 107678. https://doi.org/10.1016/j.ijmecsci.2022.107678
34. Deshpande VS, Ashby MF, Fleck NA. Foundations of topological design of truss-like lattice materials. Acta Materialia 2001; 49(6): 1035–1040. https://doi.org/10.1016/S1359-6454(00)00379-7